UNIVERSITY of CALIFORNIA
SANTA CRUZ

MORPHOLOGY OF
COMPACT LYMAN BREAK GALAXIES AT $z \simeq 3$

A thesis submitted in partial satisfaction of the
requirements for the degree of

BACHELOR OF SCIENCE

in

PHYSICS

by

Sara Mercedes Ogaz

10 June 2010

The thesis of Sara Mercedes Ogaz is approved by:

_____   _____
Professor Sandra Faber   Professor David P. Belanger
Advisor   Senior Theses Coordinator

_____
Professor David P. Belanger
Chair, Department of Physics

Abstract

Morphology of

Compact Lyman Break Galaxies at $z \simeq 3$

by

Sara Mercedes Ogaz

Star forming galaxies at high redshifts is a quickly growing area of study. These galaxies can help us understand the history of galaxy formation, and how our present day galaxies came into being. We have studied Lyman break galaxies at redshift $z \sim 3$ taken from the Hubble Great Observatories Origins Deep Survey-North using high resolution Hubble Space Telescope Advanced Camera for Surveys images. We pay particular attention to the outer parts of the galaxies. This is a difficult task given the faintness of objects at such a high redshift. To help with this we have chosen to stack the Lyman break galaxies that are selected for brightness, compactness, and roundness. After fitting stacks in the B, V, i', and z'-bands, we found that their light profiles have a best fit Sérsic index of $n \sim 4$. There is also a significant color gradient showing that the galaxy stack is red at the edge of the galaxy and blue at the center. This implies a possible age difference in the stellar populations where the outer parts of the galaxy have a population that is roughly 200 million years older than the inner parts.

Contents

In memory of my father,

David Lawrence Ogaz,

who taught me that I could accomplish anything I set my mind to.

Acknowledgements

I want to thank my advisors Sandra Faber and Kamson Lai for all of the help, advice, and support they have given me over the past year. There are no words to describe how wonderful it is to be able to work with both of you. I'd also like to thank Ian Fredrick for supplying me with amazing coffee and encouragement when I most needed it.

1 Introduction

Given the increasing resolution and capabilities of telescopes, the study of high redshift galaxies has become increasingly common. The study of galaxies at different redshifts allows us to understand galaxy evolution from the Universe's Big Bang beginning to today. In what types of galaxies does star formation occur, and how are the regions of star formation distributed within these galaxies? How do galaxies change after merging with other galaxies? What do the different types of galaxies we see today look like early in their lifetimes? These are all questions that have been asked by theorists and observers alike and much work has been done to answer them.

By studying the morphology (the overall shape and light distribution) of galaxies we can help find these answers. Morphology can reveal regions of star formation in a galaxy. We can also compare the observed morphologies of galaxies to those predicted by simulations.

Galaxies become more difficult to study the farther away from us they are. The light from distant galaxies was first emitted at a time when the Universe was only a fraction of its current age. The longer light has been traveling, the longer it has undergone expansion due to the expansion of the Universe. This expansion causes the light to become redder. The time since emission of the observed light and the distance to its source is represented by its redshift z. The higher the value of z, the more stretched and red the light has become. The galaxies we are studying are at a redshift of $z \sim 3$ and are noticeably fainter then local galaxies. We employ two different methods to overcome this. The images taken with the Hubble Space Telescope (HST) are deep images. This means that HST took very long exposures to increase the signal to noise ratio in the final image. In addition to

this we have taken *HST* images of many similar galaxies and stacked them to further improve the signal to noise ratio. For this thesis we have focused on the morphology of the compact and bright Lyman break galaxies (LBGs).

1.1   The Lyman Break Method

A significant amount of the pioneering work on high redshift ($z > 3$) LBGs was done by Charles C. Steidel in the early 1990's. The Lyman break selection method was created by Steidel as a relatively simple method of identifying galaxies at high redshift. He first published the Lyman break identification technique with Donald Hamilton in 1992 (Steidel & Hamilton 1992). There are two assumptions inherent in this technique. The first is that the astronomical object has an approximately flat spectrum in the ultra-violet part of the electromagnetic spectrum due to active star formation. The second assumption is that there is a break in the spectrum at a rest frame wavelength of 912 Å. This break occurs because of the lack of photons with wavelengths shorter than 912 Å. Within most galaxies there are few stars that emit photons at such a high energy. This is compounded by the fact that any photons that are emitted get absorbed because they are energetic enough to ionize neutral hydrogen in the stellar photosphere, the interstellar medium, and the intervening intergalactic medium along the line of sight[1].

The next step in Lyman break identification is to take images in multiple bands, having at least one band above the Lyman break and one band below. Steidel worked in three different bands at the rest wavelengths (assuming a $z \sim 3$) of U_n (λ_{rest} = 888 Å), G (λ_{rest} = 1195 Å) and $\Re$ (λ_{rest} = 1708 Å)(Steidel et al. 1996). If a galaxy is significantly dimmer in a short-wavelength image it is possible that this band falls below the Lyman break in the rest frame of the galaxy.

An example is shown in Fig. 1.1. At the top of the figure is the spectrum of an object overplotted with the throughputs of the three filters (U_n , G, and $\Re$). Near an observed wavelength of 3500 Å, there is a sudden drop in the object's spectra, the Lyman break, such that the object is

---

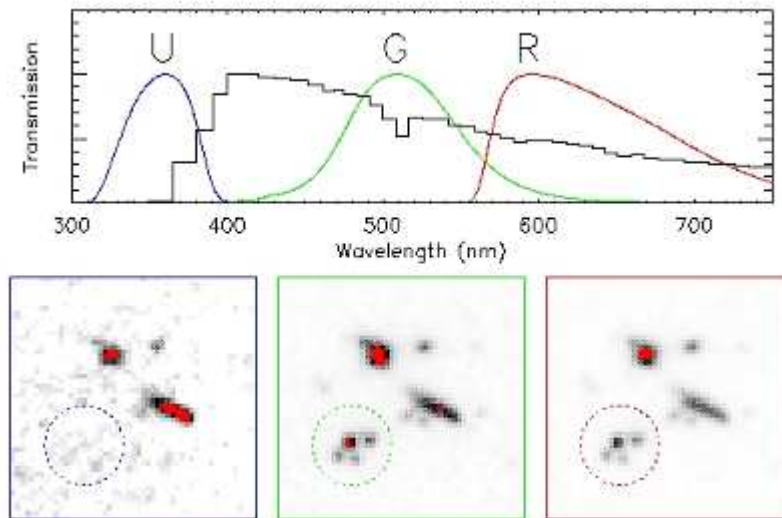[1]http://www.astro.ku.dk/~jfynbo/LBG.html

Figure 1.1: A spectrum over-plotted onto a graph of Transmission versus Wavelength in Angstroms for three filters. The three images below show a galaxy that is undetected in the U band because of the Lyman break.[2]

not visible in the U_n filter but is visible in the G and $\Re$ filters. At the bottom of the figure are three images corresponding to the three filters. A dotted circle outlines the object that is present in the G and $\Re$ filter images but absent in the the U_n filter image. Finding galaxies at a particular redshift requires at least one filter with a rest wavelength shorter than the Lyman break and one filter with a rest wavelength longer than the Lyman break. The following equation gives the observed wavelength of light at a rest wavelength $\lambda_{rest-frame}$ for a redshift z:

$$z = \frac{\lambda_{observed} - \lambda_{rest-frame}}{\lambda_{rest-frame}}.$$

Any object at the desired redshift will be undetected in the filter with the wavelength shorter than the Lyman break. The U_n, G, and $\Re$ filter set is designed for locating galaxies at a redshift of $z \sim 3$, as G and $\Re$ are longer than the Lyman break and will show light from the galaxy where as U_n is shorter than the Lyman break and will not show light from the galaxy.

In 2003 Charles C. Steidel and collaborators published a sample of 2347 galaxies in the Great Observatories Origins Deep Survey-North identified to have a redshift of $z \simeq 3$, with an apparent $\Re$ magnitude limit of 25.5. After obtaining spectra for $\sim 55\%$ of his galaxies, Steidel found

---

[2]http://www.astro.ku.dk/~jfynbo/LBG.html

that 72.5% of the spectroscopically confirmed galaxies had $z > 2$, 24% could not be matched with a redshift, and only 3.5% had $z < 2$ (Steidel et al. 2003). We can conclude from this that Steidel's method for identifying redshift is fairly robust. It is from this sample that we draw our sample for morphological study.

1.2   Morphology

One of the most powerful tools for studying galaxy morphology is the radial light profile, the distribution of light as a function of distance from the center of the galaxy. The radial profile is commonly fit with the Sérsic function(Sérsic 1963):

$$I(r) = I_e \exp\left\{-\kappa_n \left[\left(\frac{r}{r_e}\right)^{1/n} - 1\right]\right\},$$

where $I(r)$ is the surface brightness at radius r, I_e and r_e are the surface brightness and radius at the half-light radius, κ_n is a function of n such that, when $I(r)$ is integrated, half of the total light is enclosed at r_e, and n is the Sérsic index. The Sérsic index determines the shape of the model profile. Figure 1.2 shows 10 different Sérsic profiles, with n ranging from 1 to 10. A larger n gives more extended wings and a more concentrated core, while a smaller n gives a sharper decrease in light in the wings and a less concentrated core (Akiyama et al. 2008). The value $n = 1$ corresponds to an exponential profile. Disk components of nearby galaxies are typically close to exponential and have Sérsic $n < 2$. Spheroidal components of nearby galaxies are typically compact and have Sérsic $n > 4$. The value $n = 4$ is called the de Vaucouleurs profile (de Vaucouleurs 1948) and fits elliptical galaxies.

As can be seen with our LBG sample, galaxies may have one or several distinct Sérsic components. Some objects even consist of multiple clumps. These components can be circular, elliptical, or asymmetrical. In extremely asymmetrical cases, it is difficult to categorize the light distribution in a quantitative way. The Sérsic function is most appropriate for symmetrical galaxies with a single clump and a well defined center. Other methods have been developed to classify the
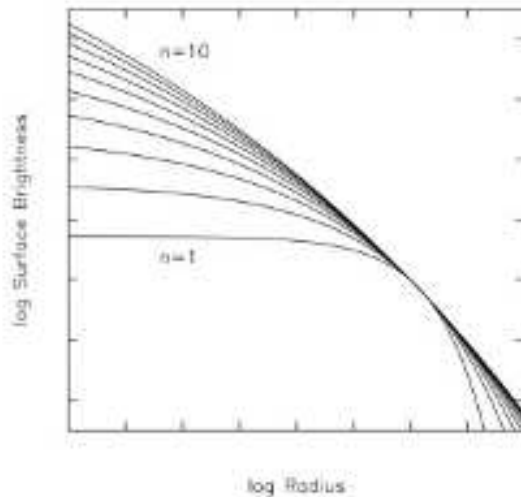
Figure 1.2: Log surface brightness vs. log radius graph[3] showing Sérsic profiles with $n = 1$ to $n = 10$

morphology of clumpy and/or asymmetrical galaxies, such as the Gini/M20 coefficients (Lotz et al. 2004). For this thesis we restrict our study to single-clump galaxies that can be easily fit with a Sérsic profile.

1.3 Previous Studies of Lyman Break Galaxies

There have been numerous previous studies on the morphology of LBGs. These studies generally found that the morphology of LBGs is extremely varied. Some galaxies have one single compact component, others have a single bright component surrounded by a fainter nebulosity, while others consist of several bright components surrounded by fainter nebulosity (Law et al. 2006). Ravindranath et al. (2006) studied 1333 LBGs from the Great Observatories Origins Deep Survey (GOODS) at $z > 2.5$, finding that $\sim 40\%$ had close to exponential light profiles (Sérsic index $n \sim 1$), $\sim 30\%$ had a high Sérsic index similar to spheroids ($n > 4$), and $\sim 30\%$ had $n < 1$. Another study by Akiyama et al. (2008) looked at individual LBGs at $z \sim 3$ with $-24.5 \leq M_v \leq -21$, where M_v is the absolute magnitude in the rest-frame V-band (observed frame K-band), and found that they had a median apparent half-light radius of 0.23" and a Sérsic index $n < 2$ using one-component fits.

---

[3] ~http://en.wikipedia.org/wiki/File:Sersic.jpg

Their sample of consisted of 31 LBGs, where 24 of the galaxies were isolated single components and 7 were multi-component. Hathi et. al (2008) used a similar stacking process to what we have used, but with LBGs at $z \simeq 4-6$. Across the redshift range studied, a Sérsic index $n < 2$ was found for all profiles. However, Hathi et al. (2008) found the profiles to deviate from this model at a radius $r \gtrsim 0.27$", which we discuss further below. Thus to summarize, previous work has found a range of Sérsic indices for high-redshift galaxies but with a tendency for the majority of objects to have low Sérsic index $(n < 2)$, especially at higher redshifts.

In our study we have looked at compact, round, single-component galaxies from Steidel's sample of $z \sim 3$ LBGs. We want to explore the light distribution of these galaxies and determine their average Sérsic index. We are especially interested in correctly measuring the fainter outside edges, a difficult task given the noise present in all astronomical images. We stack our already deep HST images in order to overcome this noise issue. One driving question is whether these compact LBGs have any diffuse light surrounding their bright cores like what is observed in the asymmetrical LBGs. There may be a significant amount of light at the edges that is currently indistinguishable from the background noise. Our data set is discussed in Section 2. In Section 3 we will discuss our methods and Section 4 our results. Finally, Section 5 presents analysis and discussion.

Table 2.1:

Exposure time for of GOODS-N ACS data

Filter	Exposure time (seconds)
B	7200
V	5650
i'	8530
z'	24760

2 Data Set

The LBG sample used in the present study came from the GOODS-North(GOODS-N) catalog of Steidel et al. (2003). We make use of the deep HST Advanced Camera for Surveys (ACS) data. The four filters used were F435W(B), F606W(V), F775W(i'), F850LP(z') corresponding to the rest wavelengths (assuming a redshift of $z = 3$) of 1000 Å, 1500 Å, 2000 Å, and 2250 Å. The throughput for each band is plotted in Fig. 2.1. The exposure time varies between bands and is shown in Table 2.1. In addition to having a higher level of background noise, the throughput in the z'-band is lower than the other bands. Therefore the total exposure time for this band is significantly higher than the other bands to achieve roughly the same signal to noise.

The images used throughout this thesis are Flexible Image Transport System (FITS) files. This format was designed for astronomical data and is the most common used in the astronomical community[4].

All of our images have been processed by the Great Observatories Origins Deep Survey (GOODS) team (Giavalisco et al. 2004). We use v2.0 GOODS-N data which have been reduced,
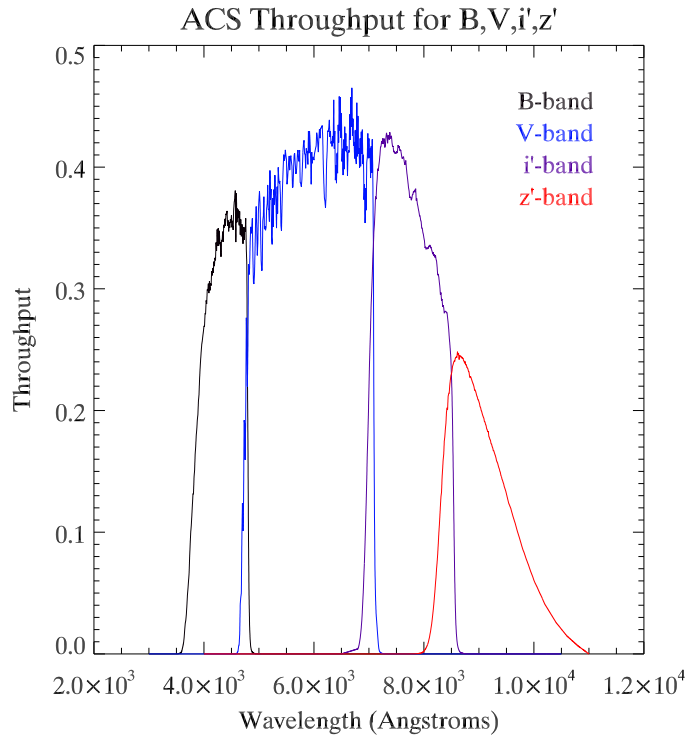
---

[4] ~http://fits.gsfc.nasa.gov/fits/home.html

Figure 2.1: Throughput for the filters[5] B, V, i' and z'. The throughput represents the sensitivity of the complete instrument (filters and CCDs)

calibrated, stacked, and mosaiced[6]. GOODS is a survey that combines deep images from the Hubble Space Telescope, the Spitzer Space Telescope, and the Chandra X-ray Observatory. The focus of the survey is to further the study of galaxy formation and evolution. The GOODS North field that we are working in extends in RA from 12h35m30s to 12h38m30s and in Dec from 62d5m0s to 62d23m0s. The GOODS-N catalog contains a total of 39,342 objects. There is one catalog for each of the four bands. Each catalog provides information such as the magnitude, ellipticity, and half-light radius of the detected objects.

---

[5] ~http://acs.pha.jhu.edu/instrument/photometry/

3 Methods

3.1 Choosing the Final Galaxy Sample

There is a large distribution of morphology types among the galaxies in the Steidel sample. Figure 3.1 shows a sample of the different types present. Starting at the left, we would classify M18 as having one bright and compact center accompanied by two diffuse components. MD27 is composed of only diffuse components. We classified C18 and MD15 as compact, round, and bright. Finally, M2 has a semi-bright center surrounded by a large diffuse component.

When choosing galaxies to stack we decided to concentrate on objects that were bright, compact, and round. By stacking these objects we can see if these compact objects are embedded in a diffuse component and learn more about their morphology. If a galaxy has a compact round core that is somewhat separated from a diffuse component or has no diffuse component (such as C15 and MD15 in Fig. 3.1), we used the galaxy but masked out the diffuse section using the Source Extractor segmentation map (explained in 3.2). This selection was done by eye. There were four cases (C11, D10, M5, and M34) where a galaxy had two clumps that were distinct, round, and compact, in which case we used both clumps as separate objects (labeled A and B) in the stack. Figure 3.2 illustrates five galaxies from our final sample of 43 galaxies. After selecting for compactness and roundness we graphed the ellipticity and full width half max of our objects against the complete GOODS-N sample in the V-band, as shown in Fig. 3.3. This confirms that we have indeed picked a subsample of objects that are comparatively compact and round.

Figure 3.1: Five different common morphologies of LBGs seen in the GOODS North field. These galaxies come from a combination of three bands (V, i' and z'). Starting from left the galaxies shown are M18, MD27, C18, MD15, and M2. M18 shows a bright and compact center embedded in a large diffuse cloud. MD27 contains no bright center, only a diffuse cloud. C18 and MD15 both contain bright round centers embedded in a small amount of diffuse matter. M2 consists of several diffuse clouds with one slightly bright core. These stamps are 3" by 3".

Table 3.1 lists the names, RA, Dec, and redshifts of our final sample of GOODS-N objects. The first name listed and the redshifts were taken from the Steidel et al.(2003) catalog, and the second name, RA, and Dec were taken from the GOODS-N catalog[6]. Table 3.2 contains the magnitudes, colors, ellipticity, and half-light radius of our final sample taken from the GOODS-N catalog. A few of the galaxies were not found or were counted as part of a bigger object in the GOODS catalog. In these cases we used magnitudes, ellipticities, and half-light radii from our own photometry catalog (see below).

We see from Table 3.1 that of the galaxies with identified redshifts, z for our galaxies ranges from $2.410 - 3.239$. Table 3.2 shows that the ellipticity of our final sample ranges from $0.035 - 0.433$ and the half-light radius from $2.339 - 7.283$ pixels, where one pixel= .03". The magnitudes in the V-band span $24.09 - 26.44$.

After choosing the final sample, we cut out stamps of 345 by 345 pixels (0.03" per pixel) from the original images centered at the galaxy's RA and Dec given by the Steidel et al. (2003) catalog.

Table 3.1:

Positions and redshifts of final sample

Name*	GOODS-N Name	RA	DEC	z_{abs}*	z_{em}*
C7	J123637.63+62104	189.1567841	62.1798477	2.658	none
C9	J123711.16+62115	189.2964783	62.1976509	none	none
C11-A	J123641.26+62120	189.1719055	62.2008553	3.214	3.222
C11-B	J123641.17+62120	189.1715393	62.2008057	3.214	3.222
C14	J123622.59+62130	189.0941162	62.2183838	none	2.981
C18	J123721.64+62135	189.3401642	62.2305984	none	3.148
C21	J123725.85+62144	189.3577271	62.2451057	none	none
C26	J123703.26+62163	189.2635803	62.2764015	3.239	none
D4	J123701.59+62105	189.2566223	62.1822624	none	none
D8	J123703.40+62115	189.2641754	62.1981430	2.410	none
D10-A	none^a	189.1956496^c	62.2072568^c	none	2.970
D10-B	none^a	189.1954891^c	62.2072331^c	none	2.970
D11	J123617.51+62130	189.0729828	62.2193413	none	2.930
D13	J123640.85+62135	189.1702118	62.2328720	3.087	none
D16	J123656.84+62172	189.2368317	62.2903938	none	none
M4	J123620.43+62093	189.0851288	62.1604614	none	none
M5-A	J123716.10+62094	189.3170776	62.1619453	none	none
M5-B	J123716.06+62094	189.3169403	62.1620560	none	none
M13	J123706.63+62113	189.2776031	62.1922035	none	none
M14	J123651.99+62115	189.2166290	62.1974754	none	none
M16	J123717.43+62124	189.3226013	62.2130051	2.939	none
M20	J123624.26+62134	189.1010895	62.2282944	none	none
M23	J123702.71+62142	189.2613068	62.2406273	3.214	none
M30	J123657.30+62162	189.2387543	62.2735558	none	none
M34-A	J123621.66+62164	189.0902405	62.2803116	none	none
M34-B	J123621.75+62164	189.0906219	62.2799683	none	none
M36	J123708.96+62172	189.2873383	62.2915115	none	none
MD3	none^b	189.1373864^c	62.1509390^c	none	2.898
MD15	J123617.77+62101	189.0740509	62.1697845	none	none
MD22	J123641.84+62110	189.1743469	62.1852875	3.191	3.197
MD25	J123632.09+62111	189.1337128	62.1884766	none	none
MD28	J123656.37+62115	189.2348785	62.1993523	none	none
MD29	J123616.70+62120	189.0695801	62.2001877	none	none
MD30	J123706.84+62120	189.2785034	62.2015953	none	none
MD33	J123629.48+62123	189.1228485	62.2088661	none	none
MD34	J123702.60+62124	189.2608337	62.2122307	none	none
MD43	J123615.50+62162	189.0645905	62.2738037	none	none
MD55	J123701.98+62172	189.2582397	62.2916069	none	none
oC14	J123650.38+62105	189.2098999	62.1819916	none	2.928
oC26	J123634.88+62125	189.1453400	62.2148476	none	3.182
oC38	J123648.84+62150	189.2035217	62.2506790	3.105	3.115
oD3	none^a	189.2012830^c	62.1643774^c	2.720	2.729
oMD24	J123709.25+62104	189.2885590	62.1798897	none	2.942

*Name and redshift (z) values determined by absorption and emission lines from Steidel et al. (2003).

^{a}These galaxies were lumped together with another component in the GOODS catalog.

^{b}This galaxy was missing from the GOODS catalog.

^{c}These data were not in the GOODS catalog and have been taken from our own Source Extractor

photometry catalogs (2σ threshold).

Table 3.2:

Photometry for final sample*

Name	V Magnitude	B-V	V-i'	i'-z'	ellipticity	half-light radius^
C7	24.525	1.130	0.370	0.108	0.169	5.378
C9	25.410	0.629	0.021	0.083	0.084	3.313
C11A	25.160	0.771	0.120	0.090	0.225	3.171
C11B	25.803	0.715	0.261	0.071	0.244	4.422
C14	25.028	0.859	0.298	0.007	0.188	4.829
C18	24.952	0.982	0.141	-0.067	0.157	3.425
C21	24.788	0.672	0.045	-0.086	0.229	3.843
C26	24.085	1.111	0.385	0.043	0.274	4.521
D4	25.567	0.767	0.237	0.246	0.396	6.691
D8	26.146	0.400	0.111	-0.204	0.091	3.830
D10A	25.578†	1.388†	0.034†	-1.603†	0.132†	4.160†
D10B	25.574†	1.473†	-0.475†	-1.672†	0.122†	4.777†
D11	25.289	0.275	-0.067	-0.100	0.074	2.909
D13	24.313	0.792	0.168	0.008	0.220	4.469
D16	25.559	0.710	0.151	0.056	0.067	4.441
M4	24.568	1.569	0.291	0.0101	0.142	3.814
M5A	25.931	0.377	0.117	-0.060	0.197	3.954
M5B	26.199	0.132	0.107	-0.028	0.293	3.255
M13	25.737	0.239	0.574	0.215	0.433	5.439
M14	25.619	1.000	0.246	0.065	0.076	3.678
M16	25.436	0.860	0.034	-0.088	0.361	4.336
M20	25.599	0.644	0.589	0.095	0.286	4.841
M23	24.509	1.018	0.358	0.192	0.270	5.326
M30	25.157	0.583	0.178	0.106	0.412	5.917
M34A	25.990	0.653	0.589	0.057	0.327	3.909
M34B	25.713	0.390	0.289	0.205	0.288	6.234
M36	25.725	2.394	0.173	-0.058	0.114	3.317
MD3	25.093†	0.935†	-0.771†	0.816†	0.072†	3.139†
MD15	24.728	0.390	0.050	-0.018	0.172	2.842
MD22	24.706	0.852	0.144	-0.039	0.094	4.049
MD25	25.467	0.156	0.194	0.282	0.221	7.283
MD28	25.363	0.114	0.027	-0.070	0.231	4.131
MD29	26.444	0.384	-0.129	0.214	0.227	3.861
MD30	25.327	1.062	0.206	0.035	0.285	4.054
MD33	25.197	0.529	0.191	-0.087	0.250	4.083
MD34	25.226	0.848	0.294	0.420	0.097	3.864
MD43	25.078	0.211	0.029	0.069	0.086	2.684
MD55	25.351	0.246	-0.026	-0.051	0.171	3.015
oC14	25.408	0.339	-0.029	-0.085	0.062	2.339
oC26	25.485	0.633	0.015	-0.279	0.242	3.631
oC38	25.051	0.985	0.248	0.020	0.134	4.445
oD3	24.914†	1.411†	-0.794†	1.078†	0.287†	3.642†
oMD24	25.787	0.777	0.192	-0.038	0.035	2.800

*Ellipticity and half-light radius from the V-band GOODS-N catalog.

^in pixel units with a scale of 0.03"/pixel.

†These data were either not in the GOODS catalog or the object was lumped with another component. The data here are taken from our own Source Extractor photometry catalogs (2σ threshold).

Figure 3.2: Five galaxies from the final sample. These galaxies come from a combination of three bands (V,i',z'). Starting from the left the galaxies shown are C7, C9, D16, M23, MD28. The stamps are 3" by 3".
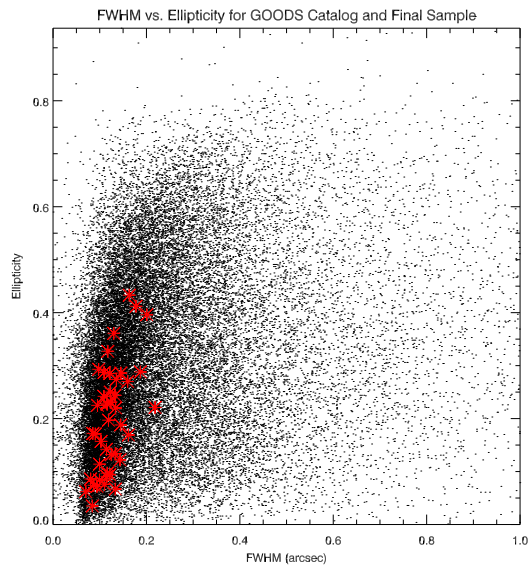

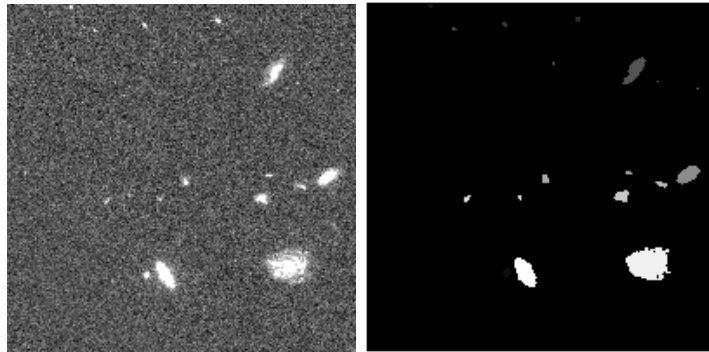Figure 3.3: Ellipticity vs half-light radius for all GOODS-N objects. Our final sample is plotted in red.

Figure 3.4: On the left is the original image and on the right is the segmentation map produced by Source Extractor. Both images are galaxy C14 in the V-band.

Table 3.3:

Average background fluctuation per pixel in surface brightness magnitude units

Band	σ	2σ	3σ
B	25.7	24.9	24.5
V	25.8	25.1	24.6
i'	25.3	24.5	24.1
z'	25.1	24.3	23.9

3.2   Source Extractor

The next step was to run Source Extractor (SE) on our GOODS-N galaxy images (Bertin & Arnouts 1996). By feeding an image and an optional weight map (an image weighting the accuracy of each pixel in the input image) along with another file defining certain parameters to SE, the program generates a catalog identifying each object it finds in the image together with measured quantities such as magnitude, ellipticity, and half-light radius. SE also generates a segmentation map image, giving an object number to the pixels identified as part of each object and giving a value of zero to the leftover pixels composing the background. Figure 3.4 shows one example of an original image stamp and the corresponding segmentation map, for galaxy C14.

Because the surface brightness of a galaxy drops off far from the center and approaches the noise level, the number of pixels counted as part of each object is highly dependent on the threshold value fed to SE. Pixel values below this threshold value are not included as part of the object. If the threshold is set too high, SE will label the edges of an object as sky pixels. If the threshold is set too low, SE will count sky as part of the object. In order to be sure that the segmentation maps used to block out other objects in our images were not too sensitive to this threshold value, we ran SE on each image with three different threshold values. This produced three different sets of photometry catalogs corresponding to three different masks for each stamp. The three threshold values were calculated from the σ of the sky background distribution: 1σ, 2σ, and 3σ. This σ was obtained by calculating the standard deviation of all pixels in each stamp (with outlier rejection), and taking the mean value of all the stamps.

---

[6]http://archive.stsci.edu/pub/hlsp/goods/catalog_r2/h_r2.0z_readme.html

3.3   Stacking the Final Sample

Stacking images is a common strategy used to increase signal to noise by averaging several images together. Once the images are aligned, pixels that are at the same pixel coordinate are added, then divided by n, where n is the number of images being stacked. So each pixel that composes the final stacked image is an average of the original n images. If most pixels at a particular position contain light from an object, the pixel value in the final image is an average value of that light. If most pixels at a particular position contain noise, because noise is random the pixel value in the final image will be close to the value of the sky background. In this way stacking images increases the ratio between the signal and noise.

Prior to stacking, several things were done to each stamp. First a background was subtracted from each FITS image (this image manipulation and all future image manipulations were done using the programming language Interactive Data Language (IDL) unless otherwise specified). An initial background value was determined for each of the three threshold values for each stamp in each band. These values were obtained by masking out any object pixels from each stamp (using the segmentation map generated by SE) and fitting the remaining pixel light histogram with a Gaussian distribution. The mean value of the fitted Gaussian was subtracted from the stamp.

Although the center pixel of the stamp contained the brightest pixel of the galaxy, the pixel itself was not exactly centered on the centroid of the galaxy. This could be an issue with stacking, and could spread the light in our final stack. To avoid this, we re-interpolated each stamp using an interpolation procedure so that the galaxy's light-weighted centroid, as determined by SE, was aligned with the center of a pixel. This means that the grid of pixels was shifted and each pixel re-averaged. We then trimmed the image so that the centroid was at the center of the image. Finally we used the segmentation maps once more to mask out all objects except the LBG by setting object pixels equal to zero but leaving in the sky background. The procedure written for this process is in Appendix A.

3.4   Background

Obtaining an accurate background value for the stamps is extremely important. We are interested in the behavior of the light profile at a large radius. The profile at this large radius is significantly affected by the background we subtract from our image because the flux value has approached the background value. As a result of this we are very careful about any background values we subtract from our final image.

Background values were subtracted at two different points in the stacking process. The first background subtraction was done as previously stated, prior to stacking with a stamp-specific background value. The second background subtraction was done to the final stacked images. For this, we took three different values for each of the twelve stacks (that is three values of threshold for each of the four bands). These three different values were obtained by taking three different regions of background pixels, shown in Fig. 3.5, from the final stacked image and calculating an average value. Table 3.4 shows the resulting background values. The values change slightly from box 3 to box 2, and change by a significant amount from box 2 to box 1.

We might have expected the background in box 1 to be brighter being close to the object and affected by object pixels, but it is actually dimmer. This is evidence that the objects do not extend into box 1 and thus are smaller than 30 pixels in radius. We also see a systematic increase in background value as the σ of the stamp increases. This is what we would expect, as a higher value of σ means that more object pixels are left in the image after masking all objects. Comparing the three different background-subtracted profiles will show the profile's dependence on this value.
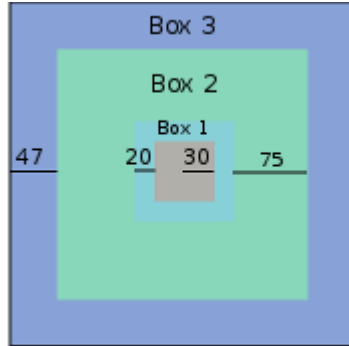
Figure 3.5: Schematic showing the three regions used to calculate background values. Light blue is box 1, light green is box 2, and the darker blue is box 3.

Table 3.4:

Background value per pixel in surface brightness units

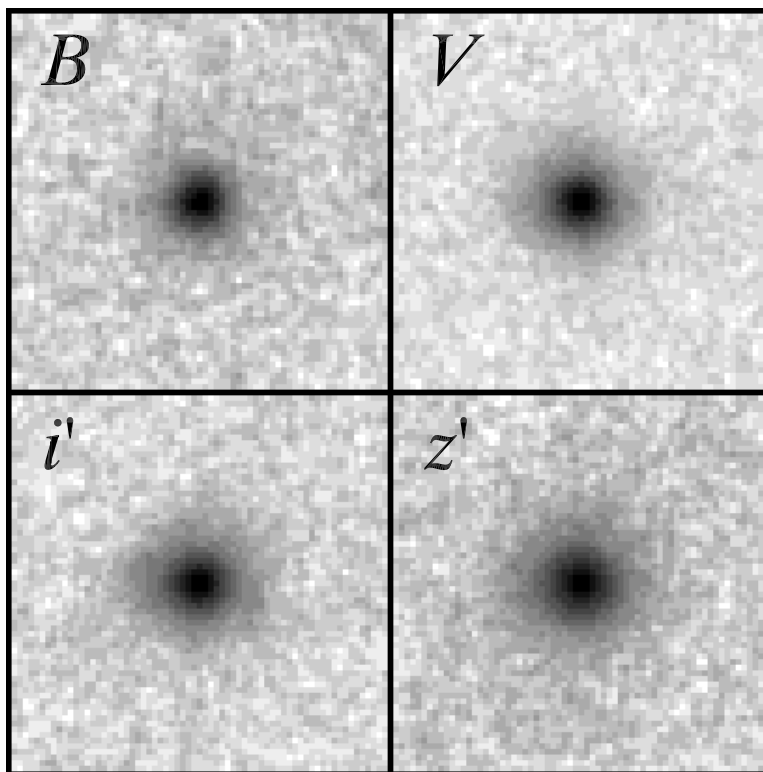|		Box 1	Box 2	Box 3
B	1σ	29.4	29.2	29.1
	2σ	29.2	29.0	28.9
	3σ	29.0	28.9	28.8
V	1σ	29.4	29.0	29.0
	2σ	29.2	28.9	28.9
	3σ	29.0	28.7	28.8
i'	1σ	29.1	28.8	28.7
	2σ	28.9	28.6	28.6
	3σ	28.7	28.4	28.4
z'	1σ	28.8	28.5	28.5
	2σ	28.3	28.1	28.2
	3σ	28.0	27.8	27.9

Figure 4.1: Final 2σ stacked images in the B, V, i', and z'. These images are 2" by 2".

4 Results

4.1 Light Profiles

Figure 4.1 contains images of the final stacks in all four bands. There is only one set of stacks shown (the 2σ set), as the results for all three σs are very similar, as discussed later in this section. We use radial light profiles to examine the final stacked images in a more quantitative way.
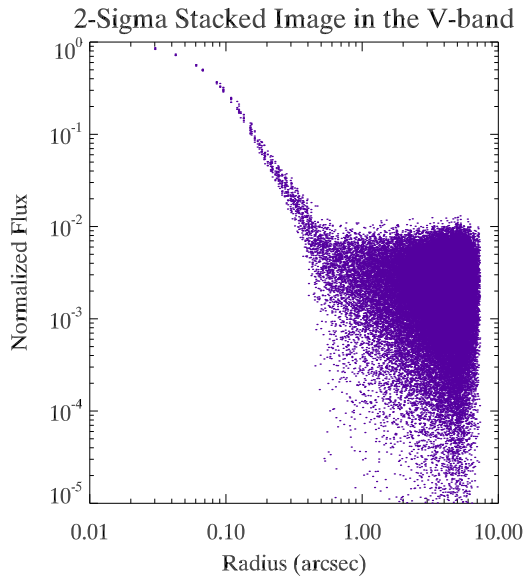
Figure 4.2: Unbinned radial profile of the 2σ stack in the V-band. The flux values have been normalized to the value of the center pixel of the stack, and only the initial background has been subtracted. Note that all pixels at a large radius are positive due to incomplete background subtraction.

For all but Fig. 4.2, we will bin all future profiles so that each plotted pixel is the average of all pixels within a a bin of $\delta r = 1$ pixel. range. Figure 4.2 is shown to illustrate the spread in the unaveraged profile plots. This profile is of the 2σ stack in the V-band. Unless stated otherwise, the profiles are normalized by dividing the entire profile by the value of the central peak pixel.

One result which we wish to emphasize is the effect of changing the background box size and threshold σ on the final radial profile of our stacked images. Figure 4.3 shows three different stacked profiles (1σ, 2σ, 3σ) with the box 3 background value subtracted in each to show the difference between σ's. We can see by comparing the profiles for all bands that for $r \leq 0.3''$ the different σ values have little effect on the radial profiles. All profiles, with the exception of the B-band fall within the error bars at $r \leq 1''$. To show the effect of changing the background box size Fig. 4.4 shows the 2σ stamp profiles with three different background boxes subtracted. The same conclusion applies here. In fact, all boxes are indistinguishable at $r \leq 0.3$ while box 2 and box 3 are indistinguishable at $r \leq 1''$. Box 1 has a radius of 30 to 50 pixels from the galaxy's center, and is rather uncertain due to a small number of pixels.
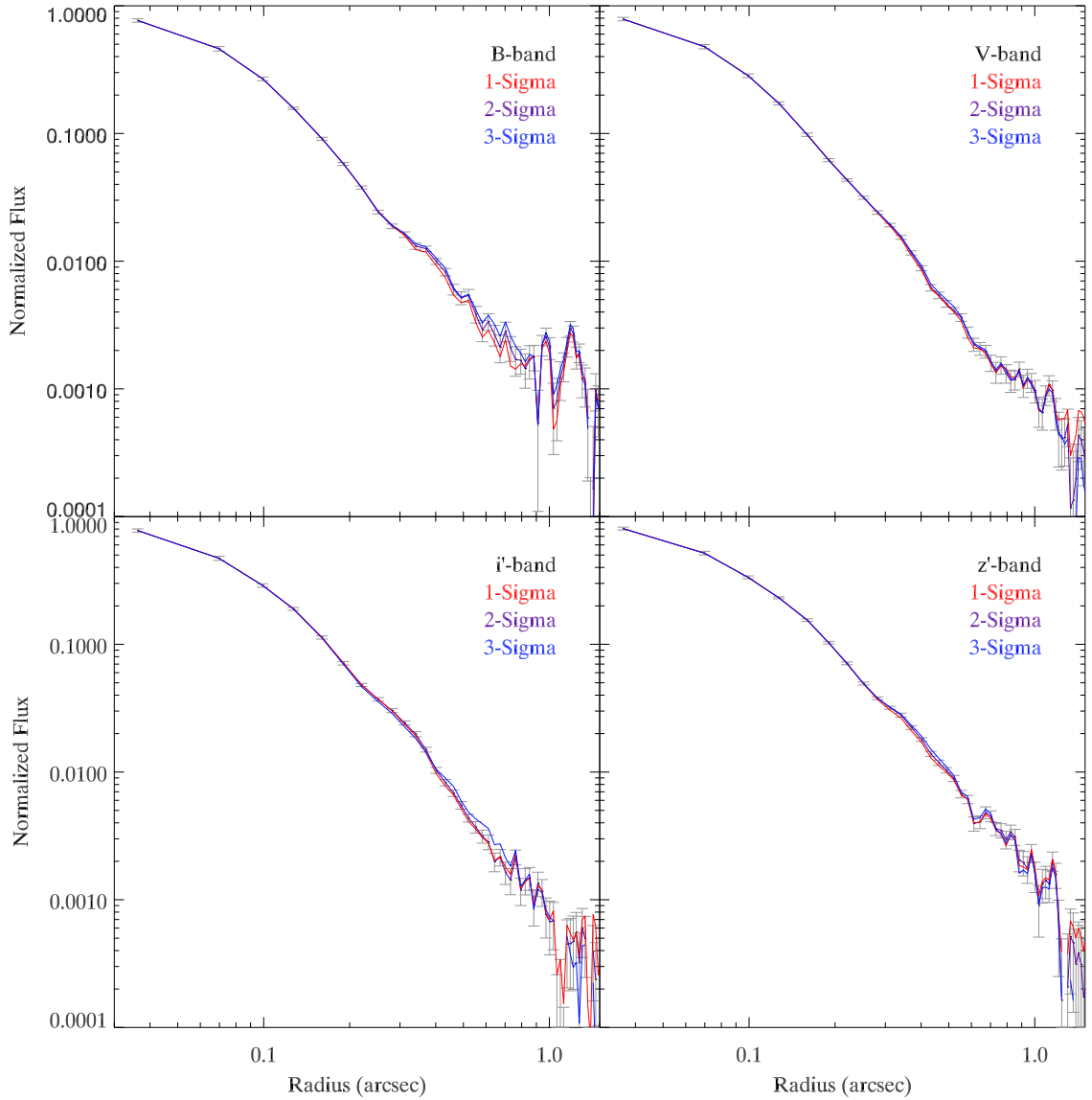
Figure 4.3: Flux vs radius graphs for all four bands. These graphs show the different profiles (with a box 3 background subtracted) using 1σ, 2σ, 3σ values while running SE. The plotted error bars represent the standard deviation of the mean pixel value being plotted. These profiles show the small effect of different σ threshold values on the shape of the profile.

Figure 4.5 shows the B, i', and z'-band radial profiles using 2σ stacks with a box 3 background subtracted) graphed together with the V-band radial profile. The excellent agreement between box 2 and box 3 suggest that we have found the proper background levels for the stacked images. We have also plotted the PSF for each band. We can see from these profiles that compared
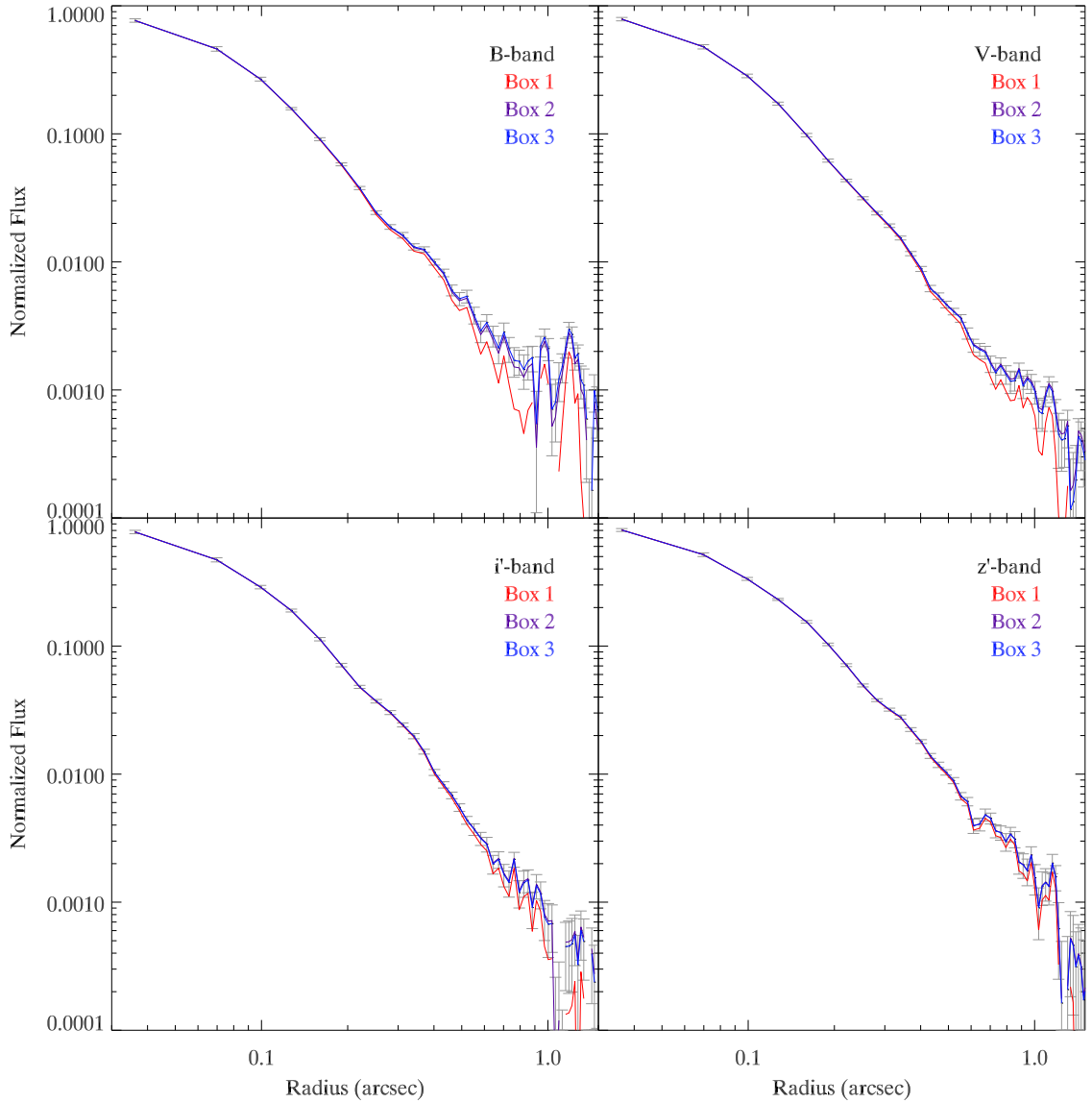
Figure 4.4: Flux vs radius graphs for all four bands. These graphs show the different profiles (using a 2σ SE threshold value) with three different background values subtracted. These three background values were determined using averages of sky pixels taken from different portions of the final stacked image. The plotted error bars represent the standard deviation of the mean pixel value being plotted. These profiles show the small effect of subtracting different background values on the shape of the profile.

to stars the galaxy stacks have a definite peak near the center and a definite tail at larger radii.

This tail approaches a straight line at larger radii in all four bands. On log-log plots a straight

line represents a power law, which has larger values at large radii than an exponential law. Thus

these profiles do not resemble a $n \sim 1$ profile (exponential disks), contrary to the results of Hathi et al. (2008). The shape of our profiles is similar to the $n \sim 4$ profiles of spheroids. Moreover by comparing the profiles in different bands we see that there are definite changes in the shape of the curve as we go to longer wavelengths. The B-band appears to have a consistently smaller flux than the V-band. The difference appears to be constant over a change in radius. Both the i' and z' bands have consistently larger fluxes than the V-band with the difference in the V-band and z'-band growing significantly with radius. As seen from the PSF profiles, a similar trend is happening in the PSF. However, we can quantify this change while accounting for the PSF effects with the Sérsic index fits produced by Galfit.

In summary, there are several conclusions we draw from the light profiles of our stacked images. The final light profiles are insensitive to reasonable changes to the background levels. This has been shown by looking at several stacks run with varying threshold values in SE, and several varying background values subtracted from the final stacks. The profiles in all four bands are very similar and show that the final image is compact but has a definite size. Beyond $\sim 0.1"$, the log-log profile closely resembles a straight line, which translates to a power law and not an exponential (exponentials are highly curved in log-log plots, see Fig. 1.2). Despite the overall similarities between colors, we do see evidence for a color gradient where the inner parts of the galaxy are blue and the outer parts red. This effect is the strongest in the V-z' color. There is the possibility that the color gradients are due to the PSFs, which show the same trends as in the final profiles. In order to quantify this we will use the Galfit in the next section to create models of the light profile that takes PSF broadening into account.

4.2   Sérsic Fits

Galfit is a software program that determines an underlying light model for a galaxy taking the point spread function (PSF) of the input image into account (Peng et al. 2002). The PSF of an image is an artifact of the telescope that spreads the light in the final image. The PSF used to
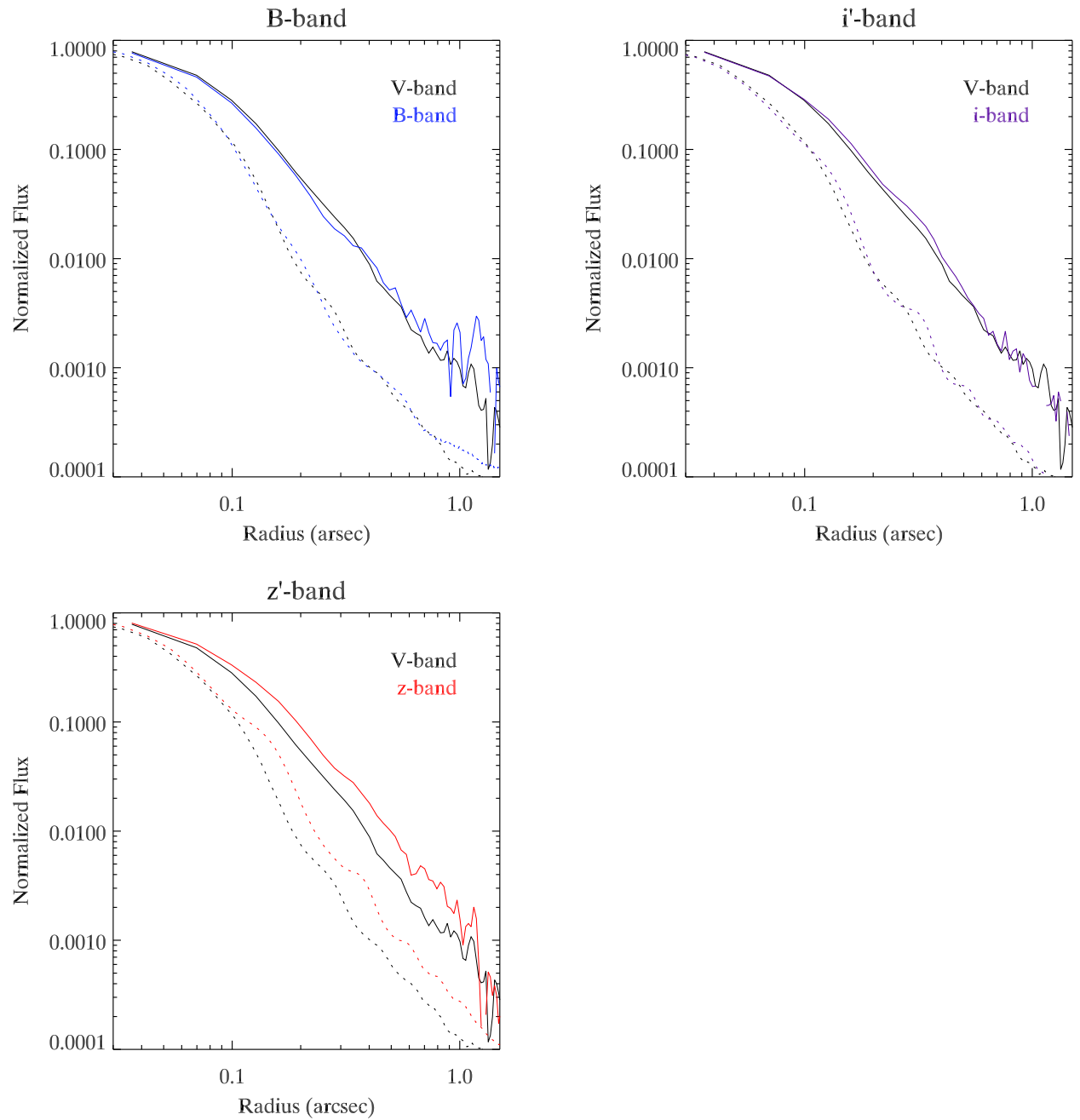
Figure 4.5: B, i', and z'-band radial profiles(solid lines) compared to the V-band radial profile and PSFs(dotted lines). Looking at the ratio between profiles from two different bands give you a color. There is a tendency for the images of the object to be brighter at redder wavelengths. However, it is also important to compare these differences to the differences between the PSFs for each band. The changes observed from band to band may be due to the change in PSF.

run Galfit was determined by stacking multiple stars in each band. These stars were taken from the GOODS-N catalog. Once a model has been determined, Galfit returns a FITS image of the model image it has fit to the galaxy as well as a text file giving output data calculated from the model. The model given by Galfit is one that has been convolved with the PSF. This means the model has been smeared the same way the original image became smeared by the PSF.

The outputs we are most interested in are the Sérsic index, half-light radius, and total magnitude. When running Galfit we used several sets of parameters. For run 1, we let Galfit fit for the Sérsic values but locked the background values at the nine values for each band previously obtained (three boxes for each of the three σ threshold values). For run 2, we ran Galfit on the 2σ stamp with the box 3 background value for each band, locking the Sérsic value at 1,2,4,6. The Sérsic index values, half light values, and magnitude are shown in Table 4.1. By comparing the quality of the fit by eye when locked to different Sérsic values, we can confirm the Sérsic value generated by Galfit in run 1. If we find that the Sérsic value from run 2 that produced the best fit is close to the Sérsic value determined from run 1, we know this value is robust.

Table 4.1 shows the Galfit results for different threshold σ's and different backgrounds. Galfit gives a Sérsic value, half-light radius, and a magnitude for each stack. Except for the B-band, the differences between profiles within each band are small, reaffirming the fact that changes in background and σ values have little effect on our final results. Figure 4.6 shows radial profiles graphed using the underlying model (model before convolution with the PSF) and the final model (model convolved with PSF) in all four bands for the 2σ stamp with a Box 3 background subtracted. Underneath each radial profile is a graph of the residuals for the fit, which shows the percent difference between the image values and the model values.

Despite the change in band, the underlying model profiles all have $n \sim 4$. This is very different from the results of both Hathi et al. (2008) and Akiyama et al. (2008). When we ran Galfit and forced a fit of $n = 1, 2, 4, 6$, we again found a value of $n = 4$ to visually best fit the stamps and to have the lowest chi squared value. The residuals of the forced fit of $n = 4$ for the V,

i',and z'-bands are below 10% up to $r \sim 0.3$" (making a conservative estimate). The residuals in the B-band are $\leq 10\%$ up to $r \sim 0.2$". Both the residuals and chi squared values confirm our Sérsic fit of $n \sim 4$.

Another striking feature of these results is the change in R_e from one band to the next. The size of one pixel in our images is 0.03", which, at redshift $z = 3$ is 1" = 7.593 kpc. From this, we calculate that $R_e = 0.583$ kpc (2.56 pixels) in the B-band and $R_e = 0.745$ kpc (3.27 pixels) in the z'-band. This is quite a large difference in radii.

Since the Sérsic values are all similar but the R_e are different, this suggests intrinsic color differences in the objects versus radius. We can confirm this by plotting the color differences in the unconvolved models for B-V, V-i', and V-z' as a function of radius, as shown in Fig. 4.7. The B-V curve has a very high value at $r \sim 0$ and *decreases* as the radius increases. The high value at small r is probably be caused by partial absorption of the B-band light by intergalactic hydrogen and does not reflect the galaxy's intrinsic stellar populations. The decreasing value at larger r is a result of a higher Sérsic fit n in B than in V. This effect may not be real; it is discussed further below. The V-z' and v-i' colors both increase from $r = 0$" to $r = 0.3$" (roughly $3 * R_e$), by 0.3-0.4 mag in V-z' and by about 0.1 mag in V-i'.

Since we want to examine the difference between bands of the flux gradients between the center of the galaxy and the outer parts of the galaxy in the *un*convolved models, Fig. 4.8 plots the following equation for B-V, V-i', and V-z':

$$(Model_1(r) - Model_1(0)) - (Model_2(r) - Model_2(0)).$$

This plot shows that the change in flux as a function of radius varies significantly between colors. If each band had the same change in flux as a function of radius, the three curves in 4.8 would be horizontal lines. As noted, B-V shows a downward trend. This decreasing value could be significant, but the Sérsic index for B is relatively uncertain. Table 4.1 shows that the variation in the Sérsic index among different choices of background boxes for the B-band is much larger than the other three bands. This means the B-band is less reliable, and the decrease we see may not reflect a true

Table 4.1: Galfit Results

Band	BKRD[a]	n[b]:1σ	n:2σ	n:3σ	R_e^c:1σ	R_e:2σ	R_e:3σ	M^d:1σ	M:2σ	M:3σ
B	1	3.57	3.78	4.03	2.17	2.21	2.29	25.69	25.68	25.66
	2	4.20	4.48	4.84	2.41	2.47	2.62	25.63	25.61	25.58
	3	4.31	4.70$*$	5.05	2.45	2.56$*$	2.72	25.62	25.59$*$	25.56
V	1	3.53	3.67	3.82	2.43	2.48	2.52	25.00	24.99	24.97
	2	3.80	3.92	4.03	2.55	2.59	2.63	24.97	24.96	24.95
	3	3.82	3.89$*$	3.98	2.56	2.58$*$	2.60	24.97	24.96$*$	24.96
i'	1	3.59	3.77	3.88	2.83	2.92	2.86	24.78	24.76	24.76
	2	3.84	3.99	4.04	2.98	3.05	2.95	24.75	24.74	24.74
	3	3.88	3.96$*$	3.96	3.01	3.03$*$	2.91	24.74	24.74$*$	24.75
z'	1	3.59	3.88	4.14	2.98	3.15	3.29	24.71	24.68	24.65
	2	3.80	4.07	4.33	3.10	3.28	4.42	24.69	24.65	24.63
	3	3.89	4.06$*$	4.21	3.16	3.27$*$	3.34	24.67	24.65$*$	24.64

*These values were our chosen final values.

[a]Background boxes

[b]Sésic index given by Galfit

[c]Half-light radius given by Galfit (in pixels)

[d]Magnitude given by Galfit

decrease in the color. The increasing trends shown in V-i' and V-z' show that the color difference is larger and growing more quickly in V-z' then V-i'. An interpretation of these results, including Fig. 4.7 and Fig. 4.8 will be discussed in the following section.
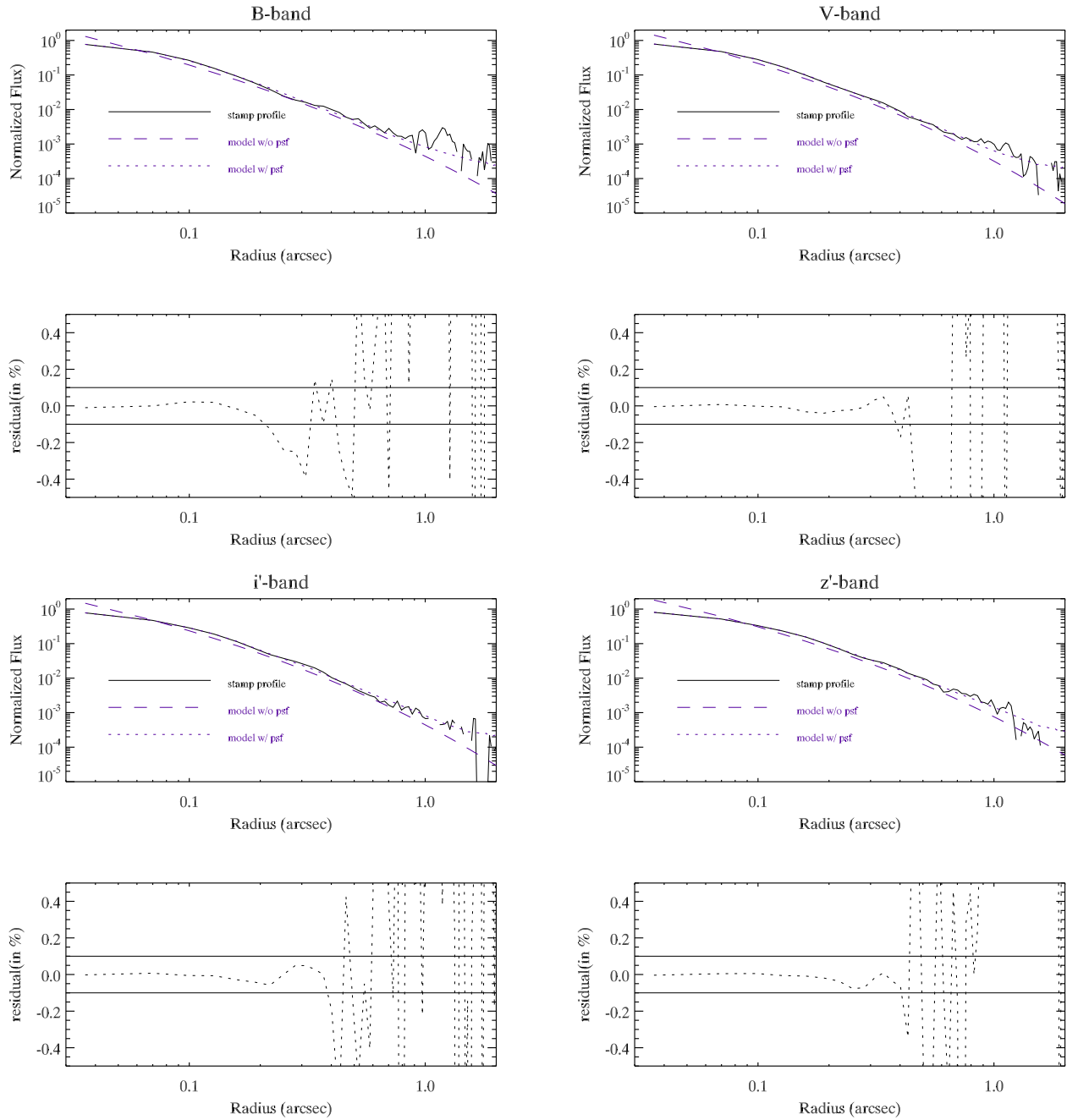
Figure 4.6: Light profile from the 2σ stack plotted with the PSF convolved model and the model without the PSF. Underneath each profile plot is a plot of the residuals of the model minus the stacked profile. These have been normalized by dividing the residual by the stack value for each pixel.
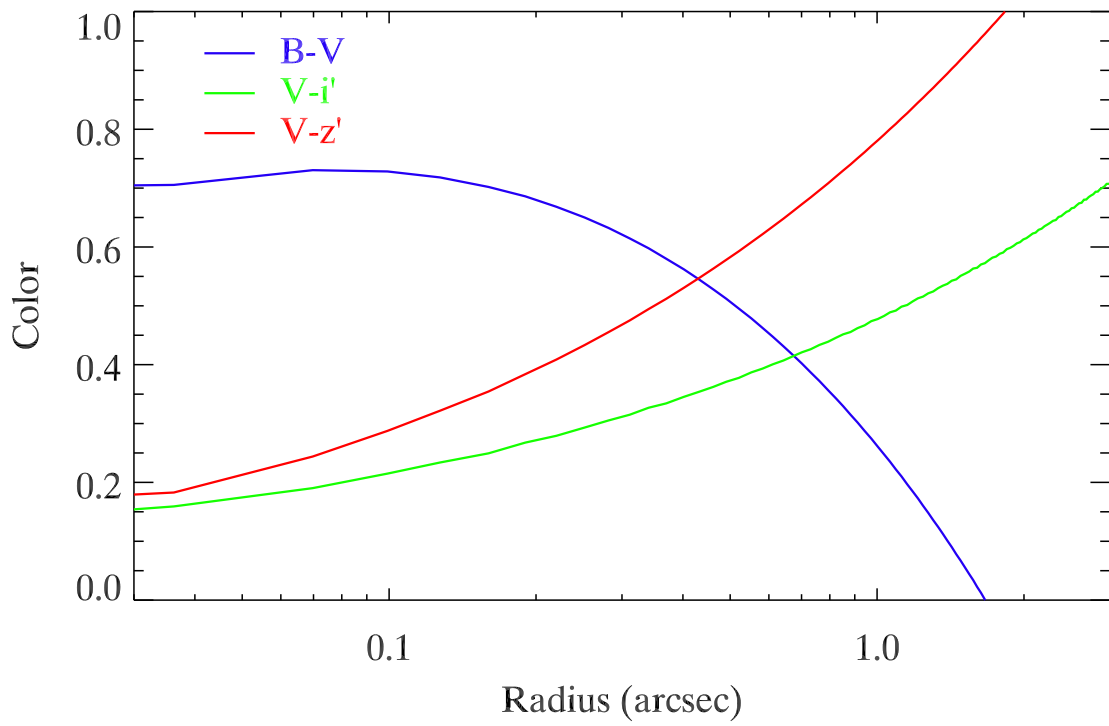
Figure 4.7: Raw models. This plot shows the color in the unconvolved models for B-V, V-i', and V-z' as a function of radius in arcseconds.
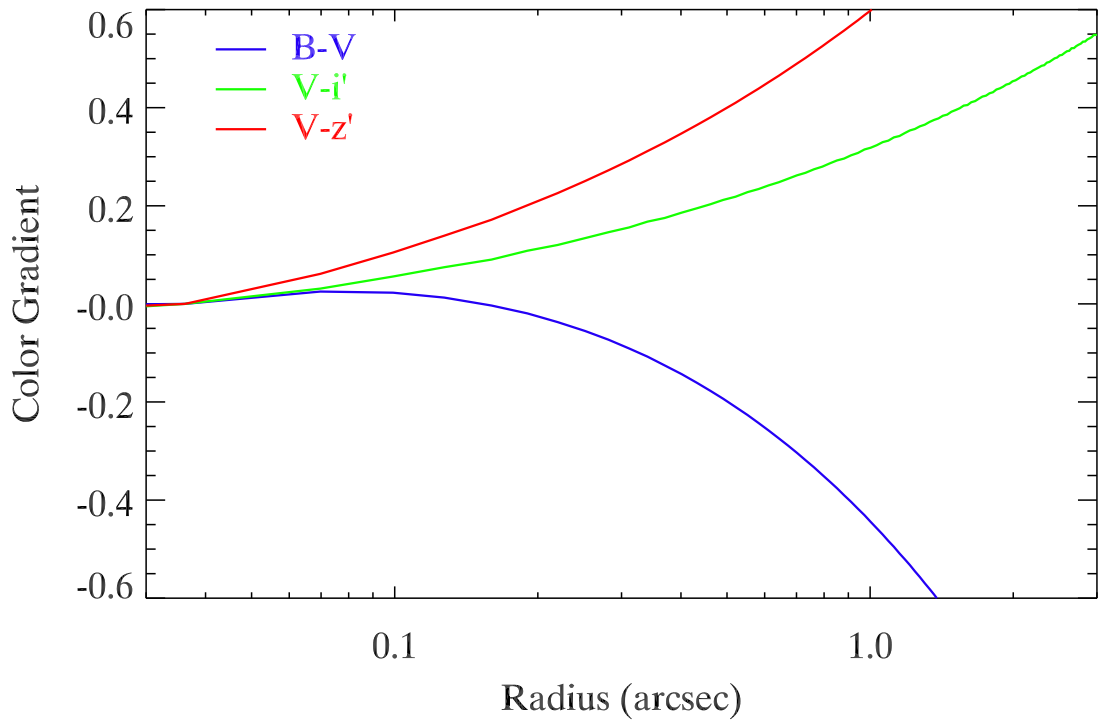
Figure 4.8: Color differences between the center of the galaxy and radius r. This plot uses the unconvolved models to show the difference between bands of the model(r)-model(0) difference in each band for B-V, V-i', and V-z'.

5 Analysis and Discussion

One of our biggest questions is why our Sérsic index $n \sim 4$ is so different from the Hathi et al. (2008) values of $n \sim 1$. One possibility is that we were looking at different types of objects. Hathi et al. (2008) were working in the Hubble Ultra Deep Field and using their own selection of dropouts. However they used a similar selection of visually bright, round, and compact galaxies and used a similar stacking process (done with 30 galaxies per stamp where we used 43 galaxies). One other possible difference is age. The galaxies of Hathi et al. (2008) range from redshift $z \sim 4$ to 6. There is a difference of at least 0.6 Gyr between these galaxies and ours. Possibly the average galaxy light profile changes significantly in that length of time.

The color gradients we find in V-i' and V-z' is new. There are three well established reasons one can find a color gradient in a galaxy. The first is metallicity. Many nearby galaxies are seen to be metal poor in the outer parts and metal rich in the inner parts (Vila-Costas & Edmunds 1992; MacArthur, Courteau & Bell 2004). But this produces a color gradient in the opposite direction of what we have found, causing the galaxy to appear redder towards the center. Another possible explanation for redness is dust. However, when dust is seen in galaxies, it is typically more prevalent in the center (Binney & Merrifield 1998; Peletier et al. 1999). Again this produces an opposite color gradient to what is seen in our galaxies.

One last possibility is star formation. A population of older stars will produce light that is more red than a population of young stars, which are quite blue. These young stars will usually dominate the UV part of the spectrum when present (Binney & Merrifield 1998, MacArthur et al.
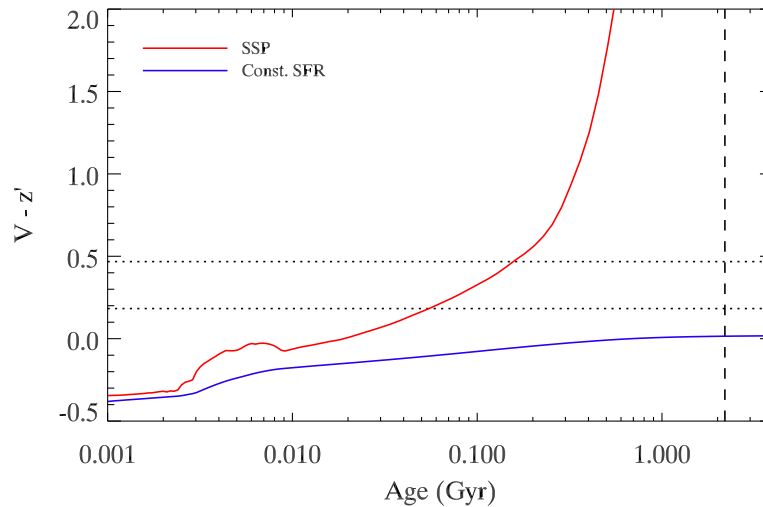
Figure 5.1: A graph showing V-z' color as a function of age (Gyr) for galaxies with a constant star formation rate, and galaxies with a single stellar population(SSP). The vertical dashed line represent the age of the Universe at $z = 3$. The two horizontal lines show the V-z' values at $r = 0$ and $r = 0.3$" for our stacked galaxies.

2004). Again our result is the opposite of what we have seen in nearby galaxies where star formation usually occurs in the outer arms of disk galaxies (Binney & Merrifield 1988). However there are nearby examples of star formation in the inner parts of galaxies, usually in mergers, which drive gas to the center, creating a central starburst. Moreover, current merger simulations show that often an old and red star population that existed in each of the two pre-merger galaxies can end up in the outer parts after the merger is complete (Lotz et al. 2008; Primack 2008). The rest result is a galaxy with young stars in the middle and older stars in the outer parts, which is what we see.

Assuming that we are seeing a reddening due to differences in star populations, we can then estimate the age difference between these populations. Figure 5.1 plots V-z' color as a function of age (Gyr) for galaxies with a constant star formation rate, and galaxies with a single stellar population(SSP). The V-z' model in Fig. 4.7 gives a value of 0.15 for $r = 0$". This translates to an age of ~ 30 Myr (assuming SSP). The V-z' color at $r = 0.3$" is about 0.5, giving an age of ~ 200 Myr. We adopt a conservative radius of 0.3" to ensure this result is robust. This is an age difference of ~ 150 Myr between the center and the outer parts of the galaxy. Keep in mind that applying

one single age to a star population is a rough estimate, and in general underestimates the mean age of stars present. Our galaxies have an approximate redshift of $z \sim 3.0$, when the Universe was ~ 2.08 Gyrs old. If the outer stellar populations is 150 Myr older than the center populations, this corresponds to a formation redshift of $z \sim 3.2$. It is entirely possible that these galaxies have been producing stars over this redshift interval.

If indeed our $n \sim 4$ Sérsic index is correct then we are looking at galaxies with profiles very similar to local spheroidal galaxies, such as ellipticals. However, one defining feature of a local spheroid is that it is old and no longer producing stars. Our galaxies are selected as LBGs because of their star formation, yet nearby star-forming galaxies have $n \sim 1$, not $n \sim 4$. So our galaxies do not fit comfortably into the local classification scheme as defined by nearby disks and ellipticals. They are different.

In future work we would like to compare the results for these compact galaxies to the other LBG morphologies. We will stack more diffuse galaxies to examine their profiles and see how they compare. We will also examine the colors of the outer parts of highly asymmetric objects to see if they are also old. Perhaps, despite the difference in appearance between these types, the distributions of stellar population ages are similar. There is also the possibility that our galaxies are post-merger remnants while the diffuse galaxies have not yet gone through a merger. There is much more we can try to understand about LBGs at this point in the evolution of the Universe and how they fit in with our population of local galaxies.

6 Appendix A

This program preforms several crucial operations to create our final galaxy stacks. First it re-interpolates the image and segmentation map produced by Source Extractor so that both will have the brightest object pixel centered on the brightest point of the galaxy. Next a background value is subtracted and the images is resized from 801x801 pixels to 345x345 pixels. The new smaller images are then masked so that any object pixel other then those of our desired object is equal to zero. Finally, all 43 galaxy images for one set (one specific band, one specific σ, one specific background box size) are stacked to produce the final image.

```
;;Created 11/2009 Last Modified: 4-30-2010  -Sara Ogaz

;;interp_center written by Kamson Lai
function interp_center,img,xc,yc,r
;; img    - input image
;; xc, yc - center of interpolation grid (IDL coords! Not fits!); do
;;          not round.
;; r      - half width of interpolation grid.  interpolated
;;          image will be 2r+1 on a side.
   gx = [xc-reverse(indgen(r)+1),xc,xc+(indgen(r)+1)]
   gy = [yc-reverse(indgen(r)+1),yc,yc+(indgen(r)+1)]
   return,interpolate(img,gx,gy,/grid,missing=0)
end


pro stack
;;read list of fits files, galaxy positions, and background values
;;(values found with gausshist.pro)
  band=['b','i','v','z']
  sigma=['1','2','3']
  readcol, '/san/deep/personal_workspaces/REU/sogaz/step2/list.txt',
  $name, x, y, format='a,x,i,i', comment='#'
  readcol, '/san/deep/personal_workspaces/REU/sogaz/step2/b_masked_dist.txt'
  $, name,b1sm,b1ss,b2sm,b2ss,b3sm,b3ss,
```

```
      $format = 'a,x,f,f,x,f,f,x,f,f', comment = '#'
      readcol, '/san/deep/personal_workspaces/REU/sogaz/step2/i_masked_dist.txt'
      $, name,i1sm,i1ss,i2sm,i2ss,i3sm,i3ss,
      $format = 'a,x,f,f,x,f,f,x,f,f', comment = '#'
      readcol, '/san/deep/personal_workspaces/REU/sogaz/step2/v_masked_dist.txt'
      $, name,v1sm,v1ss,v2sm,v2ss,v3sm,v3ss,
      $format = 'a,x,f,f,x,f,f,x,f,f', comment = '#'
      readcol, '/san/deep/personal_workspaces/REU/sogaz/step2/z_masked_dist.txt'
      $, name,z1sm,z1ss,z2sm,z2ss,z3sm,z3ss,
      $format = 'a,x,f,f,x,f,f,x,f,f', comment = '#'

;;make array of background values for for-loops  galaxies-band-sigma
    ground=[[[b1sm],[i1sm],[v1sm],[z1sm]],[[b2sm],[i2sm],[v2sm],[z2sm]]
    $,[[b3sm],[i3sm],[v3sm],[z3sm]]]

;;cycle through each postage stamp: read in appropriate files,
;;mask, interpolate, subtract background, center,
;;and resize to make new fits file
    for r=0,3 do begin
        for j=0,2 do begin
            list='/san/deep/personal_workspaces/REU/sogaz/3rdStack
            $/'+band[r]+'_1s.prt'
            imgstck=make_array(345,345,n_elements(name))
            whtstck=make_array(345,345,n_elements(name))
            for s=0,n_elements(name)-1 do begin
                original_stmp='/san/deep/personal_workspaces/REU/
      $sogaz/HDF_'+band[r]+'/'
                $+name[s]+'_'+band[r]+'.fits'
                seg_map='/san/deep/personal_workspaces/REU/sogaz/
                $graphE/segmaps/'+band[r]
                $+'/'+band[r]+sigma[j]+'s_'+name[s]+'.seg.fits'
                stacki='/san/deep/personal_workspaces/REU/sogaz/
                $step2/stacks2/'+band[r]
                $+sigma[j]+'s_allstackimg.fits'
                stackm='/san/deep/personal_workspaces/REU/sogaz/
                $step2/stacks2/'+band[r]
                $+sigma[j]+'s_allstackmed.fits'
                stackw='/san/deep/personal_workspaces/REU/sogaz/
                $step2/stacks2/'+band[r]
                $+sigma[j]+'s_allstackwht.fits'
                stacke='/san/deep/personal_workspaces/REU/sogaz/
                $step2/stacks2/'+band[r]
                $+sigma[j]+'s_allstackexp.fits'
                background=ground[s,r,j]

                old=readfits(original_stmp,h)
                wold=readfits(seg_map,he)
                num=wold[x[s],y[s]]
                gcntrd,old,x[s],y[s],xc,yc,5
                wold[where(wold eq num)]=0
                new=interp_center(old,xc,yc,172)
```

```
             new=new-background

             wnew=interp_center(wold,xc,yc,172)
             wnew=(wnew eq 0)
             blank=wnew*new

;;put new image into final array for stacking, and write new 'blank'
;;fits file
             imgstck[*,*,s]=blank
             writefits, '/san/deep/personal_workspaces/REU/sogaz/
   $step2/ifits/'
             $+band[r]+'2/'+sigma[j]+'s_'+name[s]+'_blank.fits'
             $, blank
          endfor

;;stack!
         stackimg, imgstck, fimg,fmed,fwht,fexp;
         $,whtstck=whtstck ;, maskval=0
         writefits,stacki, fimg
         writefits,stackm, fmed
         writefits,stackw, fwht
         writefits,stacke, fexp
;stop
      endfor
   endfor
return
end
```

References

[1] Akiyama, M., Minowa, Y., Kobayashi, N., Ohta, K., Ando, M. & Iwata, I. 2008, ApJ(SS), 175, 1

[2] Bertin, E. & Arnouts, S. 1996: SExtractor: Software for source extraction, Astronomy & Astrophysics Supplement 317, 393

[3] Bianchi, L., et. al. 2005, ApJ, 619, L71

[4] Binney, J. & Merrifield, M. *Galactic Astronomy*, Princeton University Press (Princeton), pg 137

[5] Bruzual, G. & Charlot, S. 2003, MNRAS, 344, 1000

[6] de Vaucouleurs, G. 1948, Ann. d'Ap., 11, 247

[7] Giavalisco, et. al. 2004, ApJ, 600, L93

[8] Gonzalez, J. J. 1993, PhD Thesis, University of California Santa Cruz

[9] Hathi, N. P., Jansen, R. A., Windhorst, R. A., Cohen, S. H., Keel, W. C., Corbin, M. R. & Ryan Jr., R. E. 2008, ApJ, 135, 156

[10] Law, D. R., Steidel, C. C., Erb, D.K., Pettini, M., Reddy, N. A., Shapley, A. E., Adelberger, K. L. & Simenc, D. J. 2007, ApJ, 656, 1

[11] Lotz, J. M., Jonsson, P., Cox, T. J. & Primack, J. R. 2008, MNRAS, 391, 1137

[12] Lotz, J. M., Primack, J., & Madau, P. 2004, AJ, 128, 163 (LPM04)

[13] Macarthur, L. A., Courteau, S., Bell, E. & Holtzman, J.A. 2004, ApJS, 152, 175

[14] Peletier, R. F., Balcells, M., Davies, R. L., Andredakis, Y., Vazdekis, A., Burkert, A. & Prada, F., 1999, MNRAS, 310, 703

[15] Peng, C. Y., Ho, L. C., Impey, C. D. & Rix, H.-W. 2002, AJ, 124, L66

[16] Ravindranath, S., et. al. 2006, ApJ, 652, 963

[17] Sérsic, J. L. 1963, Bol. Asoc. Argentina de Astron., 6, 41

[18] Steidel, C. C., Adelberger, K. L., Shapley, A. E., Pettini, M., Dickinson, M. & Giavalisco, M. 2003, Apj, 592, 728

[19] Steidel, C. C., Giavalisco, M., Pettini, M., Dickinson, M., & Adelberger & K. 1996, ApJ, 462, L17

[20] Steidel, C. C., & Hamilton, D. 1992 AJ, 104, 941, (Paper I)

[21] Vila-Costas, M. B. & Edmunds, M. G., 1992, MNRAS, 259, 121